Published in final edited form as:
Biochemistry. 2010 August 17; 49(32): 6866–6876. doi:10.1021/bi100650m.

Observation of Organometallic and Radical Intermediates Formed during the Reaction of Methyl-Coenzyme M Reductase with Bromoethanesulfonate†

Xianghui Li[#], **Joshua Telser**[‡,§], **Brian M. Hoffman**[‡], **Gary Gerfen**[⊥], and **Stephen W. Ragsdale**[*,#]

[#]Department of Biological Chemistry, University of Michigan, Ann Arbor, MI 48109

[§]Department of Biological, Chemical and Physical Sciences, Roosevelt University, Chicago IL 60605

[‡]Department of Chemistry, Northwestern University, Evanston, IL 60208

[⊥]Department of Physiology and Biophysics, Albert Einstein College of Medicine of Yeshiva University, Bronx, NY 10461

Abstract

Methyl-coenzyme M reductase (MCR) from methanogenic archaea catalyzes the final step of methane formation, in which methyl-coenzyme M (2-methylthioethane sulfonate, methyl-SCoM) is reduced with coenzyme B (N-7-mercaptoheptanolyl-threonine phosphate, CoBSH) to form methane and the heterodisulfide CoBS-SCoM. The active dimeric form of MCR contains two Ni(I)-F_{430} prosthetic groups, one in each monomer. This manuscript describes studies of the reaction of the active Ni(I) state of MCR (MCR_{red1}) with BES (2-bromoethanesulfonate) and CoBSH or its analog, CoB_6SH (N-6-mercaptohexanolyl-threonine phosphate), by transient kinetic measurements using EPR and UV-visible spectroscopy and by global fits of the data. This reaction is shown to lead to the formation of three intermediates, the first of which is assigned as an alkyl-Ni(III) species that forms as the active Ni(I)-MCR_{red1} state of the enzyme decays. Subsequently, a radical (MCR_{BES} radical) is formed that was characterized by multifrequency electron paramagnetic resonance (EPR) studies at X (~ 9 GHz)-, Q (~35 GHz)- and D (~135 GHz)-bands and by electron-nuclear double resonance (ENDOR) spectroscopy. The MCR_{BES} radical is characterized by *g*-values at 2.00340 and 1.99832 and includes a strongly coupled non-exchangeable proton with a hyperfine coupling constant of 50 MHz. Based on transient kinetic measurements, the formation and decay of the radical coincides with a species that exhibits absorption peaks at 426 nm and 575 nm. Isotopic substitution, multifrequency EPR and ENDOR spectroscopic experiments rule out the possibility that MCR_{BES} is a tyrosyl radical and indicate that if a tyrosyl radical is formed during the reaction, it does not accumulate to detectable levels. The results provide support for a hybrid mechanism of methanogenesis by MCR that includes both alkyl-Ni and radical intermediates.

†This work was supported by DOE (ER15931, SWR), NSF (MCB-0316038, BMH), and NIH (GM-075920 to GJG).

*To whom correspondence should be addressed. Stephen W. Ragsdale, Department of Biological Chemistry, University of Michigan Medical School, 1150 W. Medical Center Dr., Ann Arbor, MI 48109-0606. Tel: 734-615-4621. Fax: 734-763-4581. sragsdal@umich.edu..

[1]Deuterium signals also were not observed in the D-band (130 GHz) ENDOR spectra of samples of MCR_{red1} that had been exchanged with D_2O and incubated with BES and CoB_6SH (not shown).

BRIEFS (WORD Style “BH_Briefs”). Methyl-coenzyme M reductase forms a radical intermediate that has been characterized by spectroscopic and kinetic methods.

Keywords

Methane; methyl-Coenzyme M; methanogenesis; nickel; coenzyme F430; EPR spectroscopy; ENDOR spectroscopy; enzyme kinetics; radical

Methyl-coenzyme M reductase (MCR) from methanogenic archaea catalyzes the final step of methane formation, in which methyl-coenzyme M (methyl-SCoM, 2-methylthioethane sulfonate) is reduced with coenzyme B (CoBSH, N-7-mercaptoheptanolyl-threonine phosphate) to form methane and the heterodisulfide CoBS-SCoM according to eq1 (1,2). The structures of these substrates and analogs described in this paper are shown in Scheme 1.

$$methyl-SCoM+CoBSH \rightarrow CH_4+CoBS-SCoM \quad (1)$$

X-ray crystallographic studies have revealed that MCR is composed of three different subunits in an $(\alpha\beta\gamma)_2$ structure with an F_{430} molecule in each of the two active sites (3). Coenzyme F_{430}, a redox-active nickel tetrahydrocorphin cofactor, noncovalently binds to MCR at the bottom of a 30 Å long hydrophobic well that accommodates the two substrates and shields the reaction from solvent. The phosphate group of CoBSH is positioned by ionic interactions with MCR residues located halfway down this channel with its thiol group located 8.7 Å from the nickel. Methyl-SCoM binds in the pocket close to F_{430} such that the thioether sulfur is positioned above the nickel and about 6.4 Å from the sulfur of CoBSH. There exist various oxidation and ligation states of F_{430} in MCR, including EPR-active forms (MCR_{red1}, MCR_{red2}, MCR_{ox1} and MCR_{ox2}) (4), and EPR-silent Ni(II) forms (MCR_{silent}, $MCR_{red1\text{-}silent}$ and $MCR_{ox1\text{-}silent}$) (3,5,6). MCR_{red1} with Ni(I)-F_{430} is known to be the active form of MCR and exhibits characteristic EPR spectra with the following *g*-values: $g_\perp = 2.065$, $g_\parallel = 2.24$ (7-9).

The active MCR_{red1} state has been shown to undergo a variety of reactions, some of which lead to EPR-detectable species. In the presence of HSCoM and CoBSH, the MCR_{red1} state is partly converted into the MCR_{red2} state, which has a rhombic Ni(I)-type EPR signal (10). The reaction of MCR_{red1} with various alkyl bromides leads to the formation of organometallic alkyl-Ni species. For example, the reaction of MCR_{red1} with 3-bromopropanesulfonate (BPS), the most potent known inhibitor of methanogenesis (11), generates MCR_{PS}, (originally termed MCR_{BPS} (12)) which is an organometallic Ni(III)/propyl sulfonate species in resonance with a Ni(II)/propyl sulfonyl radical (13). The EPR spectrum of MCR_{PS} exhibits *g*-values at 2.108, 2.112, and 2.219, with most (~75%) of the spin density located in the nickel 3d(x^2-y^2) orbital (13). Similarly, when MCR_{red1} is reacted with methyl iodide or methyl bromide, an organometallic methyl-Ni(III) species is formed (MCR_{Me}) (14,15). Similar organo-Ni(III) species are generated when MCR_{red1} is reacted with various brominated acids (16). Both MCR_{Me} and MCR_{PS} can be converted to the active MCR_{red1} state under certain conditions; for example by reaction with thiolates like HSCoM (12,16,17).

While MCR_{red1} reacts with BPS to generate an organo-Ni(III) species, the reaction of MCR_{red1} with 2-bromoethanesulfonate (BES) in the presence of CoBSH generates a radical (MCR_{BES} radical), characterized by a doublet EPR signal (18). BES is a reversible inhibitor that is competitive with respect to methyl-SCoM (19,20) and has also been used to inhibit methanogenesis within the bovine rumen (21). Several other methyl-SCoM analogs, (3-bromopropionate, cyano-coenzyme M, seleno-coenzyme M and trifluoromethyl-coenzyme M), also have been shown to induce the doublet radical EPR signal when they are reacted with MCR_{red1} in the presence of CoBSH (18). The studies described in the current

manuscript were focused on obtaining a better understanding of the nature of the reaction of MCR with BES. Prior studies indicated that reactive haloalkyl compounds that are the size of HSCoM generate radicals and those that are the size of methyl-SCoM (and larger) generate organometallic species, suggesting that subtle changes in length of the reactive inhibitor (e.g., BPS versus BES) reflect the extreme selectivity in the MCR active site. However, as shown here, the reaction with BES also generates an organometallic intermediate that rapidly converts to the characteristic MCR_{BES} radical. Therefore, when comparing various haloalkanes, the nature of the intermediates actually may not change; instead the rates of formation and decay of the organometallic, radical, and other intermediates vary, thus altering the amount of these species that can accumulate.

Three types of mechanisms for MCR-based catalysis have been proposed, Mechanism I involving an organometallic methyl-Ni intermediate (6,22), Mechanism II involving a methyl radical (23) and Mechanism III, which involves methyl-Ni and interactions between the substrate and the tetrapyrrole ring of F_{430} (24). Mechanism I, proposed based on the crystal structure (3) and mechanistic work with F_{430} model complexes (25-27), involves nucleophilic attack of Ni(I)-MCR_{red1} on the methyl group of methyl-SCoM to generate a methyl-Ni intermediate (17). Mechanism III starts with protonation of coenzyme F_{430} (42), which promotes reductive cleavage of the methyl-SCoM thioether bond generating a nickel center that is coordinated by $^{-}CH_3$ and $^{-}$SCoM anions and two of the tetrapyrrole nitrogens. The $CoBS^{-}$ anion is then proposed to react with $^{-}$SCoM to form the heterodisulfide product and methyl-Ni(I). Formation of methane requires the proton that was initially donated to coenzyme F_{430}. Mechanism I is supported by the characterization of various alkyl-Ni species that have been generated by the reaction of MCR_{red1} with 3-bromopropionate (BPS) and other alkyl halides (14,16,28). In addition, MCR_{PS} and other alkyl-Ni(III) species can be converted to the active MCR_{red1} state by reacting with organic thiolates, which forms a thioether product (17). Mechanism II is based on density functional theory (DFT) computations and proposes that Ni(I) attacks the sulfur atom of methyl-SCoM, promoting homolytic cleavage of the methyl-sulfur bond and generating a MCR_{ox1}-like Ni(III)-SCoM complex and a methyl radical, which abstracts a hydrogen atom from CoBSH to generate methane (23,29,30).

Mechanisms I-III remain viable because neither the methyl-Ni(III) intermediate nor the Ni(III)-SCoM species has been observed upon reaction of MCR_{red1} with the native substrate methyl-SCoM. In fact, no spectroscopic changes have been reported when MCR_{red1} is reacted with the native substrates either separately or together, regardless of the order of addition or the concentration of the substrates. Thus, in order to probe the reaction mechanism, substrate analogs have been used. Among these, 2-bromoethanesulfonate (BES) is similar in size to methyl-SCoM and contains an excellent leaving group (Br^{-}), promoting a rapid reaction with MCR.

Here, rapid kinetic and spectroscopic experiments were performed to better understand the reaction of MCR_{red1} with BES in the presence of CoBSH or an analog, N-6-mercaptohexanolyl-threonine phosphate (CoB_6SH). The combined results indicate that formation of the MCR_{BES} radical is a three-step reaction, and that the first step involves formation of a transient alkyl-Ni(III) species that rapidly decays to form the doublet radical species. The UV-visible spectra indicate that the radical has long wavelength absorption (~550 nm). Isotopic substitution coupled with EPR and ENDOR experiments also rule out the possibility that the radical originates from one of the two Tyr residues located directly above the active site Ni center.

MATERIALS AND METHODS

Materials

Methanothermobacter marburgensis was obtained from the Oregon Collection of Methanogens (Portland, OR) catalog as OCM82. CoBSH and CoB_6SH were synthesized from 7-bromoheptanoic acid and 6-bromohexanoic acid, respectively as described previously (28,31,32). The purities of CoBSH and CoB_6SH were ascertained to be >98% by ^1H NMR. [$^2H_6$]-p-hydroxyphenylacetic acid was prepared from p-hydroxyphenylacetic acid as described (33). The yield was measured by mass spectrometry with the following distribution of deuterium: 80% of $^2H_6$-, 18% of $^2H_5$- and 2% of $^2H_4$- p-hydroxyphenylacetic acid. Other reagents were purchased from Sigma-Aldrich. N_2 (99.98%), H_2/CO_2 (80%/20%), and ultra high purity H_2 (99.999%) were obtained from Cryogenic Gases (Detroit, MI).

Protein purification

The purification of MCR_{red1} from *Mt*. marburgensis was performed under strictly anaerobic conditions, as described previously (17). According to the UV-visible spectrum (representative spectra are shown below), 50 – 70% of MCR_{red1} was typically generated. MCR_{red1}, which was universally labeled with $^2H_6$-Tyr, was generated by culturing *Mt. marburgensis* in the presence of 3 mM [$^2H_6$]-p-hydroxyphenylacetic acid, 0.1 mM phenylacetate and 0.02 mM indoleacetate, which are precursors of Tyr (*M. marburgensis* does not appear to import Tyr) (33). Peptide hydrolysis followed by mass spectrometric and amino acid analyses were used to determine the amount of [$^2H_6$]-p-hydroxyphenylacetic acid incorporated into the tyrosine residues in MCR. For amino acid analysis, MCR was hydrolyzed using 6 M HCl for 24 h at 110 °C, and then the amino residues were treated with bis-trimethylsilyl-trifluoroacetamide (BSTFA) and acetonitrile (1:1, v/v) for 1 h at 100 °C. These trimethylsilyl derivatives were analyzed using a Finnigan Trace GC/MS. O-acetylation of tyrosine in MCR was obtained through treatment of 130 μM MCR with 280 mM N-acetylimidazole on ice for 2.5 h. The excess N-acetylimidazole was removed with a molecular weight cut-off centrifugal filter.

Spectroscopy of MCR

UV-visible spectra of MCR were recorded in the anaerobic chamber using a diode array spectrophotometer (model DT 1000A, Analytical Instrument Systems, Inc., Flemington, NJ). X-band EPR spectra were recorded on a Bruker EMX spectrometer (Bruker Biospin Corp., Billerica, MA), equipped with an Oxford ITC4 temperature controller, a Hewlett-Packard model 5340 automatic frequency counter, and Bruker gaussmeter. Spin concentration was determined by double integration of the sample spectrum obtained under non-saturating conditions and comparing to that of 1 mM copper perchlorate standard. All samples for EPR spectroscopy were prepared in 50 mM Tris buffer, pH 7.6, in a Vacuum Atmospheres anaerobic chamber (Hawthorne, CA) maintained under nitrogen gas at <1 ppm of oxygen.

CW 35 GHz (“Q-band”) EPR and ENDOR (34) spectra were recorded on a modified Varian E-110 spectrometer equipped with a helium immersion dewar at 2 K under “rapid passage” (35) conditions using 100 kHz field modulation (36). Under these conditions, the EPR spectrum appears as an absorption lineshape, rather than in first derivative mode. Pulsed 35 GHz echo-detected EPR and ENDOR spectra were obtained at 2 K on a locally constructed spectrometer (37). For the echo-detected EPR spectra, the signal intensity of a standard Hahn two-pulse spin-echo is monitored as a function of field sweep. Multiple echo intensities are averaged and the EPR spectrum can be recorded at various repetition rates to probe the relaxation behavior of multiple paramagnetic sites within a sample. The lineshape

of such an echo-detected EPR spectrum may show distortions from that expected for an ideal powder pattern as the phase of the spin echo can vary during the data acquisition, due to instrumental limitations. More importantly, the T_1 is not a constant over the EPR envelope, even for a single paramagnetic site. As it is also not experimentally feasible to wait enough multiples of the longest T_1 between pulse cycles to allow full recovery of the magnetization (ideally, a repetition rate > 10 T_1), the degree of saturation and hence the intensity varies across the spectrum, distorting it. Echo-detected EPR spectra necessarily appear as the absorption lineshape, so that the 35 GHz CW and pulsed EPR spectra have the same general appearance.

For the CW ENDOR spectra (34), two methods were employed: sweeping the rf (in either direction), as is commonly done (36), or by random hopping of the rf using a sample time, delay time, and rf time, as has been recently developed (38). This latter method avoids many of the lineshape artifacts found in swept CW ENDOR spectra (39), but generally gives a lower signal/noise ratio. For the pulsed 35 GHz ENDOR spectra, the Mims three-pulse ENDOR sequence, t_{mw}-τ-t_{mw}-T(rf)-t_{mw}-τ-echo (34,40) was employed, where t_{mw} is the π/2 microwave pulse length (typically 50 ns), τ is a preparation (or delay) time (typically 500 ns), and T(rf) is the time during which the rf is applied (typically 60 μs). The Mims sequence has the property that its ENDOR intensities follow the relationship, $I(A) \sim 1 - \cos(2\pi A\tau)$, where A is the hyperfine coupling of a given nucleus. As a result, the signals vanish (give 'blind spots') at, $A\tau = n$, $n = 0, 1, \ldots$, and show maximum intensities at $A\tau = n+1/2$. However, the chief use of pulsed ENDOR in this work was to observe very weakly coupled ^{2}H signals, so that this suppression effect is of little consequence. Pulsed ENDOR measurements were implemented with random hopping of the radio frequency over the frequency range for a spectrum, a procedure that improves intensity and signal shape.

The ENDOR pattern for a single orientation of an $I = 1/2$ nucleus with relatively small hyperfine coupling and large g_N, as is the case for ^{1}H, exhibits a ν(±) doublet that is centered at the nuclear Larmor frequency, ν_N, and split by half the hyperfine coupling, $|A/2|$. For an $I = 1$ nucleus, such as ^{2}H, there is quadrupole splitting such that each hyperfine-split doublet is further split into 2I lines. However, if the hyperfine and quadrupole coupling are of similar magnitude, then this first order pattern is not obtained. For typical conditions used here: $g \sim 2.0$, $\nu_{mw} \sim 35$ GHz, $B_0 = 1.25$ T, so that $\nu(^1\text{H}) \approx 53$ MHz and $\nu(^2\text{H})) \approx 8.2$ MHz).

High Frequency (130 GHz, "D-band") EPR and ENDOR spectra were obtained on a spectrometer described previously (41,42). Field swept two-pulse (Hahn) echo-detected spectra were registered with 0/180° phase cycling of the first microwave pulse to eliminate baseline artifacts. Specific acquisition parameters are given in the figure legend.

Kinetic assay

To follow the slow kinetics related to radical decay, a diode array spectrophotometer (model DT 1000A, Analytical Instrument Systems, Inc., Flemington, NJ) was used. For observation of the rapid reaction related to radical formation, stopped-flow experiments were carried out on an Applied Photophysics spectrophotometer (SX.MV18, Leatherhead, U.K.) equipped with a photodiode array detector. The stopped-flow instrument was located in a Vacuum Atmospheres anaerobic chamber. In these mixing experiments, one syringe contained a solution consisting of 30 μM MCR_{red1} and CoBSH (or CoB_6SH), and the other contained BES. The concentrations of CoBSH (or CoB_6SH) and BES were varied in independent experiments. All experiments were performed in 50 mM Tris-HCl buffer, pH 7.6, at room temperature in the anaerobic chamber maintained at <0.5 ppm O_2. Data were globally fit using the software pro-kineticist v 1.06 (Applied Photophysics Ltd., Leatherhead, U.K.).

RESULTS

Optical Spectroscopy

Upon addition of BES to MCR_{red1} in the presence of CoB_6SH, the absorption maximum of MCR_{red1} (Fig. 1, solid line) at 385 nm shifts to 426 nm. Furthermore, the Ni(I)-associated peak at 720 nm disappears while a broad peak around 575 nm appears (dashed line), as clearly shown by the difference spectrum given in the inset. As described below, these absorption changes coincide with the formation of an EPR-active species that we will call "MCR_{BES}", or the "MCR_{BES} radical". The maximum difference absorption peaks associated with formation of the MCR_{BES} radical include a rather sharp peak at 442 nm and a broader band around 575 nm. The addition of CoB_6SH alone has no effect on the UV-visible spectrum of MCR_{red1}, while the addition of BES alone results in decay of the 385 nm and 720 nm bands of MCR_{red1} without the appearance of the absorption feature at 575 nm.

The radical species generated by the reaction of MCR_{red1} in the presence of CoB_6SH with BES is relatively stable; after one hour, the peak at 426 nm slightly decreases as the 575 nm peak disappears (Fig. 1, dotted line). The rates at which the absorption bands at 426 nm and 575 nm decrease were measured by fitting the data to a single-exponential decay function (Fig. 2), revealing a decay rate constant of $0.0021 \pm 0.0003\ s^{-1}$. When the solution containing MCR_{red1} and the native substrate CoBSH was reacted with BES, the decay rate constant was ~10-fold slower ($0.00020 \pm 0.00008\ s^{-1}$, see Fig S1, Supporting Information). Thus, the presence of the native substrate CoBSH stabilizes the MCR_{BES} radical (relative to CoB_6SH).

EPR Spectroscopy

Addition of BES to a solution of MCR_{red1}, which is characterized by *g*-values at $g_\perp = 2.065$, $g_\parallel = 2.24$ (Fig. 3A), containing CoB_6SH led to decay of the MCR_{red1} X-band EPR signal (measured at 70 K) coupled to the generation of a radical signal centered at $g \approx 2.002$ with a doublet splitting of approximately 17 G (Fig. 3B); a simulation of this signal using an isotropic ^1H hyperfine coupling of 50 MHz is also included. The peaks with values of $g_\perp = 2.16$ and $g_\parallel = 2.23$ derive from the MCR_{ox1} state, which exists in variable proportions in MCR samples and has been assigned to a Ni(III)-thiolate species in resonance with a Ni(II)-thiyl radical (43,44). There are small features at a *g* value of 2.07, which is characteristic of MCR_{red2} (45), and at g ~2.14 (of unknown origin) that are more easily resolved in the 35 GHz EPR spectrum (Figure S1, Supporting Information), but are not related to the scope of this investigation on the MCR_{BES} radical. As shown in Figure 3, the EPR signal from MCR_{ox1} is not affected by the reaction with CoB_6SH and BES, indicating that only the Ni(I) state of MCR reacts with BES in the presence of CoB_6SH. This MCR_{BES} radical signal is also observed when MCR_{red1} is reacted with BES in the presence of the native substrate, CoBSH (data not shown). As with the UV-visible experiments, both BES and CoBSH (or CoB_6SH) are required for radical formation; no changes in the MCR_{red1} EPR spectrum are observed when CoB_6SH or CoBSH alone is added, and when only BES is added, the Ni(I) state of MCR oxidizes to EPR-silent Ni(II).

To test the hypothesis that formation of the MCR_{BES} EPR signal is coupled to the UV-visible spectra with difference peaks at 442 nm and 575 nm, freeze-quench EPR experiments were performed under conditions similar to the stopped flow experiments described above (Fig. 2). Thus, when a solution of MCR_{red1} and CoB_6SH was reacted with BES, the EPR signal of the MCR_{BES} radical decayed with the same rate constant ($0.0021 \pm 0.003\ s^{-1}$) (Fig. 2, squares) that was measured by UV-visible spectroscopy (above, $0.0021\ s^{-1}$). These experiments indicate that the 575 nm peak observed in the UV-visible spectrum and the MCR_{BES} radical EPR spectrum originate from the same species.

To determine if the MCR_{BES} radical contains exchangeable protons, the reaction of MCR_{red1} with CoB_6SH and BES was carried out in both H_2O and D_2O and the resultant solutions examined by EPR and ENDOR spectroscopic experiments. As shown in Fig. 3C, the ^1H doublet splitting in the X-band EPR spectrum of the radical is unchanged when the reaction is performed in D_2O, demonstrating that the hyperfine splitting of the MCR_{BES} radical is not associated with a solvent-exchangeable hydrogen nucleus.

Accurate assignment of the *g*-values in the EPR spectra of organic radicals can aid in the identification of the radical. To obtain highly accurate *g*-values for the MCR_{BES} radical, we recorded high frequency (HF) EPR spectra at 135 GHz (D-band). This high microwave frequency has the advantage of yielding better resolution of multiple EPR-active species in a heterogeneous sample (i.e., by providing greater dispersion of *g* values) and of revealing features that permit determination of the full **g** tensor of seemingly isotropic radical centers. Although the MCR_{BES} radical appeared as a doublet with an isotropic $g = 2.00$, in the X-band EPR spectra, the Hahn echo-detected 135 GHz EPR spectrum displays approximate axial symmetry and lies entirely below $g = 2.005$ (Fig. 4). Although the majority of the spectrum appears to originate from a single radical species, it is possible that a small amount (<10%) of a minority species is present. Structure is evident in Fig. 4, but its origin is not known at this point and no attempt was made to simulate it.

Simulation of the D-band EPR spectrum yielded $g_\perp = 2.0034$ and $g_\parallel = 1.9983$. This ability to accurately determine the **g** tensor of the MCR_{BES} EPR signal in the HF spectra comes at the cost of increased linewidth due to *g*-strain (46). In the present case, the single-crystal linewidth increases from 27 MHz at X-band to 60 MHz at D-band, so that the 17 G splitting evident in the X-band spectra (Fig. 1A) is no longer resolved (simulations of the D-band spectrum were almost identical whether or not an isotropic ^1H hyperfine splitting of 50 MHz, as determined at X-band, was included). Likewise, the resolved ^{14}N hyperfine splitting at $g_\perp$ of the MCR_{red1} signal (from the F_{430} pyrrole/pyrroline ligands (43,45)) evident in the X-band spectrum is not resolved in the 135 GHz or the 35 GHz spectra (see Fig. S2, Supporting Information).

Q-Band (35 GHz) and D-Band (135 GHz) ENDOR spectroscopic experiments

The 35 GHz ENDOR methodology employed here uses a temperature of 2 K, which is best suited to metal-centered paramagnets. Thus, it was comparatively easy to record good quality spectra on field positions of the MCR Ni signals (e.g., $g \sim 2.17$), which readily showed the ν_+ partner of the strongly coupled ($A(^1H) = 28$ MHz) signal that has been attributed to a hydrido ligand (denoted H_{rh}) to Ni(III) in MCR_{red2a} (47). This signal can be seen in Fig. 5. In this case, CW ENDOR with random hopping of the rf was employed, which gives a better baseline. A corresponding swept ENDOR spectrum is shown in Figure S3 (Supporting Information). In contrast, spectra recorded at the field position of the radical signal ($g \sim 2.00$) were of lower signal/noise ratio and did not exhibit any strongly coupled protons; only those with $A(^1H) < \sim 12$ MHz were observed, as also seen in Fig. 5. Swept rf CW ^1H Q-band ENDOR spectra recorded at $g \sim 2.00$ (radical signal) and at $g \sim 2.17$ (MCR signal) are shown in Fig. S3. Under these conditions, the ^1H ENDOR signal has a higher signal/noise ratio. There appear to be signals extending to > 20 MHz from $\nu(^1H)$, so that the maximum hyperfine coupling may be > 40 MHz, in agreement with the X-band EPR results. Note that at 35 GHz, the radical EPR signal still appears isotropic (in contrast to the 130 GHz result, Fig. 4). As a result, there is no “orientation selection” in the ENDOR, in contrast to the anisotropic MCR signal(s), which leads to broader ENDOR lines and greater difficulty in determining the $\mathbf{A}(^1H)$ tensor. No significant differences were seen in the ^1H pattern for H_2O versus D_2O samples.

The use of ^{2}H ENDOR facilitates focusing on the question of solvent exchange more directly. Fig. 5 (inset) compares the 35 GHz Mims ^{2}H ENDOR spectra of the MCR_{BES} samples generated in H_2O and D_2O, recorded at the field position corresponding to the maximum intensity of the radical signal. The sample in D_2O showed a largely unresolved matrix ^{2}H ENDOR signal centered at the ^{2}H Larmor frequency that is essentially the same when recorded at varying field positions on the EPR envelope of the radical signal. Superimposed on this is a poorly resolved splitting, which might be assigned to $A(^2H) \approx 0.3$ MHz (corresponding to $A(^1H) \approx 2$ MHz, which is well inside the overall ^{1}H CW ENDOR pattern, Fig. S1).1 In summary, the combined ENDOR and EPR results rule out the possibility that the doublet splitting seen in the X-band EPR spectrum derives from an exchangeable proton.

Isotopic substitution and EPR/ENDOR spectroscopic experiments to determine if the MCR_{BES} species derives from a tyrosyl radical

Based on the crystal structure of MCR (3), there are a number of viable candidates for the relatively stable MCR_{BES} radical. These include: αTyr333 (4.3 Å from Ni), βTyr367 (4.3 Å from Ni), αthioglycine445 (12 Å from Ni), the sulfur of CoBSH (8.87 Å away from Ni) (6) or the corphin ring itself. Given how close αTyr333 and βTyr367 are to the Ni active site, they seemed to be the most likely contenders.

Tyrosyl radicals are widely found in enzymes, including the photosynthetic oxygen evolving complex (OEC) (48,49), prostaglandin H synthase (PGHS) (50,51), ribonucleotide reductase (RNR) (52) and galactose oxidase (53,54). The low frequency (X-band) EPR spectra of tyrosyl radicals are dominated by hyperfine coupling to non-exchangeable protons. Each of the two ring protons ortho to the phenol oxygen have an anisotropic coupling, the largest component of which is typically in the 20 to 30 MHz range. The two side-chain methylene protons have an approximately isotropic coupling, the values of which are highly dependent on the dihedral angle with respect to the ring plane normal. Depending on the angle, the coupling of these protons may range from ~ 0 to > 60 MHz. However, no matter what the angle, at least one methylene proton will experience a significant (>10 MHz) hyperfine coupling. The variability of the side chain dihedral angle, and resulting variability of the methylene proton hyperfine couplings, means that the X-band spectra of tyrosyl radicals can display a variety of splitting patterns. But all tyrosyl radical spectra experience significant spectral splittings and/or width from the hyperfine coupling of 3 or 4 non-exchangeable protons, and thus the substitution of natural abundance tyrosine by an isotopolog that is

[1]Abbreviations

MCR	Methyl-coenzyme M reductase
BES	bromoethane sulfonate
BPS	3-bromopropanesulfonate
DFT	density functional theory
ENDOR	electron nuclear double resonance
EPR	electron paramagnetic resonance
HF	high frequency
HSCoM	Coenzyme M
CoBSH	Coenzyme B
rf	radiofrequency

deuterated at *any* position would be expected to have an observable spectral impact for any tyrosyl radical species.

Unlike X-band spectra, the D-band spectra of tyrosyl radicals are dominated by the (field-dependent) Zeeman interaction, which is gauged by *g*-values. Unmodified tyrosyl radicals have an anisotropic (rhombic) g-matrix with principal values that are fairly consistent: g_x (or g_1) is in the range of 2.009 −2.006 depending on the electrostatic/hydrogen bonding environment of the phenol oxygen; g_y (or g_2) ~2.004 - 2.005; and g_z (or g_3) ~ 2.002 - 2.003. Thus, by using HFEPR to determine the *g*-values, as well as X-band EPR and Q-band ENDOR to measure the hyperfine couplings of the radical in the enzyme prepared with both protonated and deuterated tyrosine, we sought to provide definitive evidence for or against the radical species originating from tyrosine, specifically αTyr333 or βTyr367.

Samples of MCR were generated that contained a tyrosine isotopolog. MCR_{red1} was globally labeled with $^2H_6$-Tyr by feeding *M. marburgensis* cells with $^2H_6$-hydroxyphenylacetate; then MCR was isolated and digested, and the amino acids were analyzed with GC-MS. The results showed that at least 50% of tyrosine residues in MCR were labeled with $^2H_4$-Tyr instead of $^2H_6$-Tyr. This is a lower estimate of the labeling percentage because significant H-exchange occurs during the acid hydrolysis. A similar estimate of the labeling percentage was obtained by mass spectrometric analysis of BrCN- and AspN-digested fragments of MCR isolated from cells grown on labeled hydroxyphenylacetate, e.g., greater than 50% of βTyr367 was labeled (Fig. 6). Even though the fragment including αTyr333 was not identified, eleven other peptides containing tyrosine residues showed a similar percentage of $^2H_6$-Tyr labeling. Thus, independent amino acid and peptide analyses confirmed that the Tyr residues in MCR were significantly labeled when cells were fed with $^2H_6$-hydroxyphenylacetate under the conditions described.

In order to test the hypothesis that the radical intermediate detected by EPR and UV-visible spectroscopic studies derives from Tyr, $^2H_6$-Tyr-labeled MCR_{red1} was reacted with BES in the presence of CoB_6SH. If the EPR spectra were associated with one of the two Tyr residues located immediately above the Ni center at the active site of MCR, then a significant change in the lineshape would be expected upon substitution of these $^1H_6$-Tyr residues with $^2H_6$-Tyr. As shown in Fig 3D, the EPR spectrum of the MCR_{BES} radical appeared unchanged by the ^2H-Tyr substitution, with the same degree of hyperfine splitting remaining in the MCR_{BES} radical. These experiments unambiguously rule out the possibility that MCR_{BES} contains a tyrosyl radical.

Pulsed 35 GHz ENDOR spectra of the sample containing $^2H_6$-Tyr exhibited a very weak and featureless signal centered at the deuteron Larmor frequency. Essentially the same signal (not shown) was observed at multiple positions on the EPR envelope. This ^2H signal may arise from distant coupling to the various paramagnetic centers that make up the overall EPR envelope. The ^1H ENDOR spectrum of this sample was indistinguishable from the samples with natural abundance tyrosine whether in H_2O or D_2O solvent.

Effect of tyrosyl acetylation

Even though the EPR experiments clearly show that MCR_{BES} radical is not a tyrosyl radical, the tyrosyl residues still appear to play an important role in radical formation. As shown in Fig 7A, acetylation of tyrosyl residues in MCR_{red1} by treatment with N-acetylimidazole has no effect on the EPR spectrum of MCR_{red1}; however, Tyr acetylation blocks the formation of the MCR_{BES} radical. As shown in Fig 7C, the amount of MCR_{BES} generated from the reaction of acetylated MCR_{red1} with BES and CoB_6SH was greatly decreased and some MCR_{red1} remains, as compared with the reaction of unlabeled MCR_{red1} with BES and CoB_6SH (Fig. 7B).

Kinetics of MCR_{BES} radical formation

The MCR_{BES} radical is formed rapidly and the transient kinetics were followed by stopped-flow with UV-visible spectroscopy (Fig 8A). The kinetic data ranging from 350 nm to 732 nm were globally fit to a four-component equation (eq 2). Two spectral intermediates, B (Fig 8B, red line),

$$A \xrightarrow{k_1} B \xrightarrow{k_2} C \xrightarrow{k_3} D \qquad \text{eq 2}$$

C (Fig 8B, blue line) and D (associated with the MCR_{BES} radical) were identified. The difference spectra between A and B (Fig 8B inset, black line) showed that a new species with absorption at 420 nm and a shoulder at 457 nm was formed accompanying the decay of the 385 and 720 nm bands of MCR_{red1}. It has been shown that the shoulder around 457 nm is characteristic of the methyl-Ni(III) species of MCR (14); thus, we assign intermediate B as an alkyl-Ni(III) species. The 457 nm peak then disappears as intermediate B converts to intermediate C, which appears to be a Ni(II) species. In the last step, the MCR_{BES} radical (Species D) forms.

By varying the concentration of BES (Fig 9A) or CoB_6SH (Fig 9B), the first step in this three-step sequence (with rate constant k_{obs1}) was shown to be dependent on the concentrations of both CoB_6SH and BES, while k_{obs2} and k_{obs3} were independent of the CoB_6SH or BES concentrations. The k_{obs1} was fit to equation 3 to derive the values of k_1 and K_m, where [S] is the concentration of CoB_6SH or BES.

$$k_{obs1} = \frac{k_1 \times [S]}{K_m + [S]} \qquad \text{eq 3}$$

The rate constants for the three steps are provided in Table 1. The conversion of A to intermediate B gives a second order rate constant of 45,000 $M^{-1}s^{-1}$, the conversion of intermediate B to C has a rate constant of 2.6 s^{-1} and formation of the MCR_{BES} radical (species D) occurs with a rate constant of 1.0 s^{-1}. As shown above, decay of Species D occurs with a rate constant of 0.0021 s^{-1} (not given in Table I).

DISCUSSION

Transient kinetics combined with UV-visible and EPR spectroscopic experiments have revealed the accumulation of three intermediates during the reaction of the active Ni(I)-MCR_{red1} with the substrate analogs CoB_6SH and BES (Figure 8). Figure 10 describes the mechanism by which the various species form. The first of these intermediates is assigned as an alkyl-Ni(III) species because it exhibits an absorption spectrum similar to that of the organonickel intermediates formed when MCR_{red1} reacts with various alkyl halides including BPS and methyl iodide (14,17). When reacted with thiolates (including HSCoM) (12,16,28), these alkyl-Ni(III) species convert to the active MCR_{red1} state along with the corresponding alkane when protonolyzed or reduced with Ti(III) citrate (14,17), supporting the catalytic intermediacy of the alkyl-Ni species in methane synthesis. Prior studies indicated that reactive haloalkyl compounds that are the size of HSCoM generate radicals, while those that are the size of methyl-SCoM (and larger) yield organometallic species. However, as shown here, the reaction with BES also generates an organometallic intermediate that rapidly converts to the characteristic MCR_{BES} radical. Therefore, the reaction of MCR with all haloalkanes may generate an initial organometallic species that converts to other intermediates at varying rates that determine whether or not these species accumulate to detectible levels. This organonickel species (B) quickly converts to a

relatively stable radical labeled as X· in Figure 8 (Species D, MCR_{BES}) through Intermediate C, which was identified by global kinetic analysis. We propose that MCR_{BES} is formed by homolytic cleavage of the alkyl-Ni(III) bond to generate an unstable alkyl radical that would abstract a hydrogen atom from the precursor of X· (i.e., X-H).

Free radicals have been identified as intermediates in a number of enzymatic reactions (55). These radicals include amino acid-based radicals, such as the tyrosyl radical in class I ribonucleotide reductases (52) and in other enzymes (49,51,53), a cysteine-based thiyl radical in all three classes of ribonucleotide reductase (55), and a glycyl radical in pyruvate formate lyase (56). Furthermore, catalytic radicals are formed by various cofactors, e.g., the adenosyl radical (generated from S-adenosyl-L-methionine or adenosylcobalamin), a hydroxyethyl thiamine pyrophosphate radical in pyruvate ferredoxin oxidoreductase, and a porphyrin π-cation radical in chloroperoxidase (55,57,58).

Radicals have been proposed as key intermediates in the MCR-catalyzed synthesis of methane (6,22,23); however, so far such radicals have not been identified spectroscopically when MCR is reacted with its natural substrates. On the other hand, a radical EPR doublet signal (the MCR_{BES} radical) is generated when MCR_{red1} is reacted with BES in the presence of CoB_6SH/CoBSH (18). We show here that MCR_{BES} is transiently formed and accumulates to a maximum of ~20 % of the initial amount of MCR_{red1}.

Based on the crystal structure of MCR (3), it appears that several amino acids (Tyr and thioglycine), the corphin ring itself, and the sulfur group of its substrates, CoB_6SH/CoBSH or HSCoM, are reasonable candidates for XH, the precursor of the MCR_{BES} radical. Although the simplest explanation for the 575 nm absorption peak and the MCR_{BES} radical to accumulate over the same time frame is that they belong to the same species, another possibility is that the EPR and UV-visible spectra belong to different, but kinetically coupled, species. This is because transient kinetic experiments assign intermediates based on the dynamics of spectral evolution. For example, homolytic cleavage of alkyl-Ni(III) would generate the alkyl radical and a Ni(II) species, which would be assigned as a single intermediate by the global kinetic fitting protocol, because they form and decay at the same rate. According to this scenario, the UV-visible spectrum would be dominated by the Ni(II) component and the EPR spectrum would reveal the radical. As described above, because two Tyr residues are situated just above the upper axial Ni ligand (the ethyl sulfonyl group in this case), we used EPR and ENDOR spectroscopy to test the possibility that the MCR_{BES} radical comes from Tyr.

Our EPR and ENDOR spectroscopic studies of the MCR_{BES} radical generated from $^2H_6$-Tyr-labeled MCR rule out the possibility that the MCR_{BES} radical derives from tyrosine. First, the *g*-values of the MCR_{BES} radical ($g_\perp$ = 2.0034 and $g_\parallel$ = 1.9983) are not consistent with those typically observed for a Tyr radical which exhibits rhombic spectra with g_1 is in the range of 2.009 to 2.006, g_2 at 2.004 - 2.005 and g_3 at 2.002 - 2.003. The *g*-values of the MCR_{BES} radical are most consistent with a species with significant electron spin density localization on carbon, hydrogen and/or nitrogen rather than oxygen and sulfur, since the latter would be expected to result in *g* values > 2.005 (for sulfur-based radicals, see (59-61)). Furthermore, as described in the Results section, because all tyrosyl radical spectra exhibit significant broadening or splitting from the hyperfine interactions of 3 or 4 non-exchangeable protons, the substitution of natural abundance Tyr by ^{2}H-Tyr would be expected to markedly alter the spectrum of any tyrosyl radical species. The lack of any observable difference in the EPR spectra of the MCR_{BES} radical generated from enzyme containing ^{2}H- versus ^{1}H-Tyr demonstrates conclusively that MCR_{BES} is not a Tyr radical.

The visible spectrum, with a broad peak around 575 nm, is also inconsistent with a typical Tyr radical. For example, the primary absorption bands characteristic for a phenoxyl radical include a sharp intense band at ~410 nm ($\varepsilon > 1800\ M^{-1}cm^{-1}$), another intense but broader band at ~390 nm ($\varepsilon > 900\ M^{-1}cm^{-1}$) and a broad weak band at ~600 nm ($\varepsilon < 500\ M^{-1}cm^{-1}$) (62,63). Although the absorption spectrum is not consistent with a Tyr radical, it would not be inconsistent with that of a radical formed on the corphin ring of F_{430}. A porphyrin π-radical, which is coupled with an oxoiron(IV) heme species, has been reported in many hemoproteins (57) and has a characteristic absorbance in the range of 650 to 700 nm (64). Because the corphin ring contains only five double bonds, four of which are in conjugation, the absorption maxima of a corphin-based radical could shift to higher energies. However, as mentioned below, the EPR spectra are inconsistent with assigning the radical to the tetrapyrrole ring of F_{430}. Alternatively, as mentioned above, one can consider the possibility that the EPR and UV-visible spectra belong to different, but kinetically coupled, species.

Glycyl, tryptophanyl, ketyl, allyl and other C/N based radicals as well as the corphin-based radical may have *g* values in the range observed here, but these species have hyperfine couplings that are either not fully characterized or are inconsistent with those measured here. For example, although it is an otherwise attractive possibility given the long wavelength absorption (see below), it appears highly unlikely that the MCR_{BES} radical derives from the corphin ring of F_{430} because the Ni(II) center in MCR and in the free cofactor has an $S = 1$ configuration with a significant zero field splitting (65). Thus, such a radical would likely magnetically interact with the tetrapyrrole in a way that would lead to a significantly different EPR spectrum that that observed. Rather than being a narrow EPR signal at $g \approx 2.00$, a coupled radical would have substantial *g* anisotropy. It appears that the observed EPR spectrum could only arise from a tetrapyrrole-centered radical if the Ni(II) center were in the $S = 0$ configuration, which has no precedence in MCR forms. Thus, although a Tyr radical can be ruled out, further experiments, including isotopic substitutions, will be required to make a positive assignment for the MCR_{BES} radical.

Even though MCR_{BES} (X· in Figure 10) does not contain a tyrosyl radical, our results suggest that a tyrosyl residue may still play a role in formation of the MCR_{BES} radical. Acetylation of tyrosyl residues greatly inhibits the reaction of MCR_{red1} with BES, suggesting that a tyrosyl residue may be involved in formation of MCR_{BES} radical. The acetyl group may simply sterically hinder the reaction of Ni(I) with BES and MCR_{BES} may be formed by a pathway independent of the involvement of Tyr. However, another hypothesis that is consistent with our Tyr-modification results is that the stable doublet MCR_{BES} radical with the long wavelength absorbance is generated by hydrogen atom abstraction from a transient Tyr radical. According to this scenario, the ethanesulfonyl radical (Intermediate C) could abstract a hydrogen atom from one of the two nearby Tyr residues to form a tyrosyl radical that could rapidly abstract a hydrogen atom from the corphin ring or one of the other species described above (CoBSH/CoB_6SH, thiogycine, HSCoM) to generate the MCR_{BES} radical (Species D). In this scenario, the Tyr radical would form and decay too rapidly to accumulate to detectable levels. The intermediacy of the Tyr radical is, of course, speculative since, thus far, the only radical we have observed is the relatively stable MCR_{BES} radical with the doublet EPR spectrum.

The detection of both organonickel and radical species suggests a new mechanism for methane synthesis that combines the key features of Mechanisms I (a methylnickel intermediate) and II (a methyl radical intermediate). Both mechanisms also predict that a thiyl-radical from CoBSH is generated as an intermediate, but the EPR parameters of the MCR_{BES} radical do not support a thiyl radical assignment for the doublet EPR signal. Because of the inhibitory effects of Tyr acetylation, we speculate that the stable radical is formed by abstraction of a H-atom from an initially formed Tyr radical. The final proposed

steps in both Mechanisms I and II involve a disulfide anion radical (CoBS-SCoM) that reduces the Ni(II) species (above) back to active MCR_{red1}. Our studies also provide evidence against a potential F_{430}-based radical, which was invoked in Mechanism III.

Because no intermediates have been observed in various rapid kinetic studies of the reaction of MCR_{red1} with the native substrates, it is important to identify the MCR_{BES} radical by performing further isotope labeling studies. Recent experiments of the reaction of MCR_{red1} with methyl-SCoM and CoB_6SH reveal a doublet radical, but with different UV-visible spectra than those of MCR_{BES} (unpublished, Dey & Ragsdale). Thus, experiments similar to those described here may reveal the identity of an intermediate in the reaction with methyl-SCoM and CoBSH.

Supporting Informational material is available free of charge via the Internet at http://pubs.acs.org and contains the following: Kinetics of MCR_{BES} radical decay with BES and CoBSH as substrates (Figure S1), 35 GHz EPR spectra at 2 K of MCR_{red1} in presence 1 mM CoB_6SH after addition of BES (Figure S2), and Broad scan swept CW 35 GHz ^1H ENDOR spectra of MCR_{red1} recorded at 2 K at a field position on the MCR signal (g = 2.177, upper trace) and on the radical signal (g = 2.002, lower trace) (Figure S3).

Supplementary Material

Refer to Web version on PubMed Central for supplementary material.

REFERENCES

1. DiMarco AA, Bobik TA, Wolfe RS. Unusual coenzymes of methanogenesis. Annu Rev Biochem. 1990; 59:355–394. [PubMed: 2115763]
2. Thauer RK. Biochemistry of methanogenesis: a tribute to Marjory Stephenson. 1998 Marjory Stephenson Prize Lecture. Microbiology. 1998; 144(Pt 9):2377–2406. [PubMed: 9782487]
3. Ermler U, Grabarse W, Shima S, Goubeaud M, Thauer RK. Crystal structure of methyl-coenzyme M reductase: the key enzyme of biological methane formation. Science. 1997; 278:1457–1462. [PubMed: 9367957]
4. Mahlert F, Bauer C, Jaun B, Thauer RK, Duin EC. The nickel enzyme methyl-coenzyme M reductase from methanogenic archaea: In vitro induction of the nickel-based MCR-ox EPR signals from MCR-red2. J Biol Inorg Chem. 2002; 7:500–513. [PubMed: 11941508]
5. Grabarse W, Mahlert F, Shima S, Thauer RK, Ermler U. Comparison of three methyl-coenzyme M reductases from phylogenetically distant organisms: unusual amino acid modification, conservation and adaptation. J Mol Biol. 2000; 303:329–344. [PubMed: 11023796]
6. Grabarse W, Mahlert F, Duin EC, Goubeaud M, Shima S, Thauer RK, Lamzin V, Ermler U. On the mechanism of biological methane formation: structural evidence for conformational changes in methyl-coenzyme M reductase upon substrate binding. J Mol Biol. 2001; 309:315–330. [PubMed: 11491299]
7. Goubeaud M, Schreiner G, Thauer RK. Purified methyl-coenzyme-M reductase is activated when the enzyme-bound coenzyme F_{430} is reduced to the nickel(I) oxidation state by titanium(III) citrate. Eur J Biochem. 1997; 243:110–114. [PubMed: 9030728]
8. Albracht SPJ, Ankel-Fuchs D, Böcher R, Ellermann J, Moll J, van der Zwann JW, Thauer RK. Five new EPR signals assigned to nickel in methyl-coenzyme M reductase from *Methanobacterium thermoautotrophicum*, strain Marburg. Biochimica et Biophysica Acta. 1988; 955:86–102.
9. Rospert S, Böcher R, Albracht SPJ, Thauer RK. Methyl-coenzyme M reductase preparations with high specific activity from H_2-preincubated cells of Methanobacterium thermoautotrophicum. FEBS Lett. 1991; 291:371–375. [PubMed: 1657649]
10. Goenrich M, Duin EC, Mahlert F, Thauer RK. Temperature dependence of methyl-coenzyme M reductase activity and of the formation of the methyl-coenzyme M reductase red2 state induced by coenzyme B. J Biol Inorg Chem. 2005; 10:333–342. [PubMed: 15846525]

11. Ellermann J, Rospert S, Thauer RK, Bokranz M, Klein A, Voges M, Berkessel A. Methyl-coenzyme-M reductase from *Methanobacterium thermoautotrophicum* (strain Marburg). . Purity, activity and novel inhibitors. Eur. J. Biochem. 1989; 184:63–68. [PubMed: 2506016]
12. Rospert S, Voges M, Berkessel A, Albracht SP, Thauer RK. Substrate-analogue-induced changes in the nickel-EPR spectrum of active methyl-coenzyme-M reductase from Methanobacterium thermoautotrophicum. Eur J Biochem. 1992; 210:101–107. [PubMed: 1332856]
13. Hinderberger D, Piskorski RP, Goenrich M, Thauer RK, Schweiger A, Harmer J, Jaun B. A nickel-alkyl bond in an inactivated state of the enzyme catalyzing methane formation. Angew Chem Int Ed Engl. 2006; 45:3602–3607. [PubMed: 16639771]
14. Dey M, Telser J, Kunz RC, Lees NS, Ragsdale SW, Hoffman BM. Biochemical and spectroscopic studies of the electronic structure and reactivity of a methyl-Ni species formed on methyl-coenzyme M reductase. J Am Chem Soc. 2007; 129:11030–11032. [PubMed: 17711283]
15. Yang N, Reiher M, Wang M, Harmer J, Duin EC. Formation of a nickel-methyl species in methyl-coenzyme M reductase, an enzyme catalyzing methane formation. J Am Chem Soc. 2007; 129:11028–11029. [PubMed: 17711279]
16. Dey M, Kunz RC, Lyons DM, Ragsdale SW. Characterization of alkyl-nickel adducts generated by reaction of methyl-coenzyme m reductase with brominated acids. Biochemistry. 2007; 46:11969–11978. [PubMed: 17902704]
17. Kunz RC, Horng YC, Ragsdale SW. Spectroscopic and kinetic studies of the reaction of bromopropanesulfonate with methyl-coenzyme M reductase. J Biol Chem. 2006; 281:34663–34676. [PubMed: 16966321]
18. Goenrich M, Mahlert F, Duin EC, Bauer C, Jaun B, Thauer RK. Probing the reactivity of Ni in the active site of methyl-coenzyme M reductase with substrate analogues. J Biol Inorg Chem. 2004; 9:691–705. [PubMed: 15365904]
19. Gunsalus RP, Romesser JA, Wolfe RS. Preparation of coenzyme M analogues and their activity in the methylcoenzyme M reductase system of *Methanobacterium thermoautotrophicum*. Biochemistry. 1978; 17:2374–2377. [PubMed: 98178]
20. Ellermann J, Hedderich R, Böcher R, Thauer RK. The final step in methane formation. Investigations with highly purified methyl-CoM reductase (component C) from *Methanobacterium thermoautotrophicum* (strain Marburg). Eur. J. Biochem. 1988; 172:669–677. [PubMed: 3350018]
21. Immig I, Demeyer D, Fiedler D, Van Nevel C, Mbanzamihigo L. Attempts to induce reductive acetogenesis into a sheep rumen. Arch. Tierernahr. 1996; 49:363–370. [PubMed: 8988318]
22. Signor L, Knuppe C, Hug R, Schweizer B, Pfaltz A, Jaun B. Methane formation by reaction of a methyl thioether with a photo-excited nickel thiolate--a process mimicking methanogenesis in archaea. Chemistry. 2000; 6:3508–3516. [PubMed: 11072815]
23. Pelmenschikov V, Blomberg MR, Siegbahn PE, Crabtree RH. A mechanism from quantum chemical studies for methane formation in methanogenesis. J Am Chem Soc. 2002; 124:4039–4049. [PubMed: 11942842]
24. Duin EC, McKee ML. A New Mechanism for Methane Production from Methyl-Coenzyme M Reductase As Derived from Density Functional Calculations. J Phys Chem B. 2008
25. Lin S-K, Jaun B. Coenzyme F430 from Methanogenic bacteria: detection of a paramagnetic methylnickel(II) derivative of the pentamethyl easter by ^{2}H-NMR spectroscopy. Helvetica Chimica Acta. 1991; 74:1725–1738.
26. Lin S-K, Jaun B. Coenzyme F430 from Methanogenic bacteria: mechanistic studies on the reductive cleavage of sulonium ions catalyzed by F430 pentamethyl ester. Helvetica Chimica Acta. 1992; 75:1478–1490.
27. Lahiri, Goutam K.; Schussel, Leonard J.; Stolzenberg, AM. F430 model chemistry. Mechanistic investigation of the reduction, coupling, and dehydrohalogenation of alkyl halides by the nickel(I) octaethylisobacteriochlorin anion. Inorganic chemistry. 1992; 31:4991–5000.
28. Kunz RC, Dey M, Ragsdale SW. Characterization of the thioether product formed from the thiolytic cleavage of the alkyl-nickel bond in methyl-coenzyme M reductase. Biochemistry. 2008; 47:2661–2667. [PubMed: 18220418]
29. Pelmenschikov V, Siegbahn PE. Catalysis by methyl-coenzyme M reductase: a theoretical study for heterodisulfide product formation. J Biol Inorg Chem. 2003; 8:653–662. [PubMed: 12728361]

30. Chen SL, Pelmenschikov V, Blomberg MR, Siegbahn PE. Is there a Ni-methyl intermediate in the mechanism of methyl-coenzyme M reductase? J Am Chem Soc. 2009; 131:9912–9913. [PubMed: 19569621]
31. Bobik TA, Wolfe RS. Physiological importance of the heterodisulfide of coenzyme M and 7-mercaptoheptanoylthreonine phosphate in the reduction of carbon dioxide to methane in Methanobacterium. Proc Natl Acad Sci U S A. 1988; 85:60–63. [PubMed: 3124103]
32. Noll KM, Donnelly MI, Wolfe RS. Synthesis of 7-mercaptoheptanoylthreonine phosphate and its activity in the methylcoenzyme M methylreductase system. J Biol Chem. 1987; 262:513–515. [PubMed: 3100513]
33. Porat I, Sieprawska-Lupa M, Teng Q, Bohanon FJ, White RH, Whitman WB. Biochemical and genetic characterization of an early step in a novel pathway for the biosynthesis of aromatic amino acids and p-aminobenzoic acid in the archaeon Methanococcus maripaludis. Mol Microbiol. 2006; 62:1117–1131. [PubMed: 17010158]
34. Telser, J. Electron-Nuclear Double Resonance (ENDOR) Spectroscopy. In: Scott, RA.; Lukehart, CM., editors. Applications of Physical Methods to Inorganic and Bioinorganic Chemistry. John Wiley & Sons; Chichester, UK: 2007. p. 99-124.
35. Mailer C, Taylor CPS. Rapid adiabatic passage EPR of ferricytochrome c. Signal enhancement and determination of the spin-lattice relaxation time. Biochimica et Biophysica Acta. 1973; 322:195–203. [PubMed: 4358082]
36. Werst MM, Davoust CE, Hoffman BM. Ligand Spin Densities in Blue Copper Proteins by Q-band ^{1}H and ^{14}N ENDOR Spectroscopy. Journal of the American Chemical Society. 1991; 113:1533–1538.
37. Davoust CE, Doan PE, Hoffman BM. Q-Band Pulsed Electron Spin-Echo Spectrometer and Its Application to ENDOR and ESEEM. Journal of Magnetic Resonance. 1996; 119:38–44.
38. Lee H-I, Igarashi RY, Laryukhin M, Doan PE, Dos Santos PC, Dean DR, Seefeldt LC, Hoffman BM. An Organometallic Intermediate during Alkyne Reduction by Nitrogenase. Journal of the American Chemical Society. 2004; 126:9563–9569. [PubMed: 15291559]
39. Doan PE, Gurbiel RJ, Hoffman BM. The Ups and Downs of Feher-Style ENDOR. Appl. Magn. Reson. 2007; 31:647–661.
40. Schweiger, A.; Jeschke, G. Principles of Pulse Electron Paramagnetic Resonance. Oxford University Press; Oxford, UK: 2001.
41. Krymov V, Gerfen GJ. Analysis of the tuning and operation of reflection resonator EPR spectrometers. J Magn Reson. 2003; 162:466–478. [PubMed: 12810032]
42. Ranguelova K, Girotto S, Gerfen GJ, Yu S, Suarez J, Metlitsky L, Magliozzo RS. Radical sites in Mycobacterium tuberculosis KatG identified using electron paramagnetic resonance spectroscopy, the three-dimensional crystal structure, and electron transfer couplings. J Biol Chem. 2007; 282:6255–6264. [PubMed: 17204474]
43. Harmer J, Finazzo C, Piskorski R, Bauer C, Jaun B, Duin EC, Goenrich M, Thauer RK, Doorslaer SV, Schweiger A. Spin Density and Coenzyme M Coordination Geometry of the ox1 Form of Methyl-Coenzyme M Reductase: A Pulse EPR Study. J. Am. Chem. Soc. 2005; 127:17744–17755. [PubMed: 16351103]
44. Craft JL, Horng Y-C, Ragsdale SW, Brunold TC. Nickel Oxidation States of F_{430} Cofactor in Methyl-Coenzyme M Reductase. Journal of the American Chemical Society. 2004; 126:4068–4069. [PubMed: 15053571]
45. Finazzo C, Harmer J, Jaun B, Duin EC, Mahlert F, Thauer RK, Doorslaer SV, Schweiger A. Characterization of the MCR_{red2} form of methyl-coenzyme M reductase: a pulse EPR and ENDOR study. J. Biol. Inorg. Chem. 2003; 8:586–593. [PubMed: 12624730]
46. Hyde JS, Froncisz W. The Role of Microwave Frequency in EPR Spectroscopy of Copper Complexes. Ann. Rev. Biophys. Bioeng. 1982; 11:391–417. [PubMed: 6285804]
47. Harmer J, Finazzo C, Piskorski R, Ebner S, Duin EC, Goenrich M, Thauer RK, Reiher M, Schweiger A, Hinderberger D, Jaun B. A Nickel Hydride Complex in the Active Site of Methyl-Coenzyme M Reductase: Implications for the Catalytic Cycle. J. Am. Chem. Soc. 2008; 130:10907–10920. [PubMed: 18652465]

48. Dorlet P, Valentin MD, Babcock GT, McCracken JL. Interaction of $Y_Z\cdot$ with Its Environment in Acetate-Treated Photosystem II Membranes and Reaction Center Cores. J. Phys. Chem. B. 1998; 102:8239–8247.
49. Hoganson CW, Babcock GT. Protein-tyrosyl radical interactions in photosystem II studied by electron spin resonance and electron nuclear double resonance spectroscopy: comparison with ribonucleotide reductase and in vitro tyrosine. Biochemistry. 1992; 31:11874–11880. [PubMed: 1332777]
50. Shi W, Hoganson CW, Espe M, Bender CJ, Babcock GT, Palmer G, Kulmacz RJ, Tsai A.-l. Electron Paramagnetic Resonance and Electron Nuclear Double Resonance Spectroscopic Identification and Characterization of the Tyrosyl Radicals in Prostaglandin H Synthase 1. Biochemistry. 2000; 39:4112–4121. [PubMed: 10747802]
51. Dorlet P, Seibold SA, Babcock GT, Gerfen GJ, Smith WL, Tsai A.-l. Un S. High-Field EPR Study of Tyrosyl Radicals in Prostaglandin H_2 Synthase-1. Biochemistry. 2002; 41:6107–6114. [PubMed: 11994006]
52. Hoganson CW, Sahlin M, Sjöberg B-M, Babcock GT. Electron Magnetic Resonance of the Tyrosyl Radical in Ribonucleotide Reductase from *Escherichia coli*. J. Am. Chem. Soc. 1996; 118:4672–4679.
53. Whittaker JW. Free Radical Catalysis by Galactose Oxidase. Chem. Rev. 2003; 103:2347–2364. [PubMed: 12797833]
54. Gerfen GJ, Bellew BF, Griffin RG, Singel DJ, Ekberg CA, Whittaker JW. High-Frequency Electron Paramagnetic Resonance Spectroscopy of the Apogalactose Oxidase Radical. J. Phys. Chem. 1996; 100:16739–16748.
55. Stubbe J, van Der Donk WA. Protein Radicals in Enzyme Catalysis. Chem Rev. 1998; 98:705–762. [PubMed: 11848913]
56. Wagner AF, Frey M, Neugebauer FA, Schafer W, Knappe J. The free radical in pyruvate formate-lyase is located on glycine-734. Proc Natl Acad Sci U S A. 1992; 89:996–1000. [PubMed: 1310545]
57. Sono M, Roach MP, Coulter ED, Dawson JH. Heme-Containing Oxygenases. Chem. Rev. 1996; 96:2841–2888. [PubMed: 11848843]
58. Frey PA, Hegeman AD, Reed GH. Free radical mechanisms in enzymology. Chem Rev. 2006; 106:3302–3316. [PubMed: 16895329]
59. Symons MCR. On the electron spin resonance detection of RS radicals in irradiated solids: radicals of type $RSSR^-$, $RS\text{-}SR^{+\,2}$, and $R_2SSR_2^+$ J. Chem. Soc., Perkin Trans. 2. 1974:1618–1620.
60. Gastel, M. v.; Lubitz, W.; Lassmann, G.; Neese, F. Electronic Structure of the Cysteine Thiyl Radical: A DFT and Correlated ab Initio Study. J. Am. Chem. Soc. 2004; 126:2237–2246. [PubMed: 14971960]
61. Lassmann G, Kolberg M, Bleifuss G, Gräslund A, Sjöberg B-M, Lubitz W. Protein thiyl radicals in disordered systems: A comparative EPR study at low temperature. Phys. Chem. Chem. Phys. 2003; 5:2442–2453.
62. Larsson A, Sjoberg BM. Identification of the stable free radical tyrosine residue in ribonucleotide reductase. EMBO J. 1986; 5:2037–2040. [PubMed: 3019680]
63. Petersson L, Graslund A, Ehrenberg A, Sjoberg BM, Reichard P. The iron center in ribonucleotide reductase from Escherichia coli. J Biol Chem. 1980; 255:6706–6712. [PubMed: 6248531]
64. Svistunenko DA. Reaction of haem containing proteins and enzymes with hydroperoxides: the radical view. Biochim Biophys Acta. 2005; 1707:127–155. [PubMed: 15721611]
65. Cheesman MR, Ankel-Fuchs D, Thauer RK, Thomson AJ. The magnetic properties of the nickel cofactor F430 in the enzyme methyl-coenzyme M reductase of *Methanobacterium thermoautotrophicum*. Biochem. J. 1989; 260:613–616. [PubMed: 2504147]

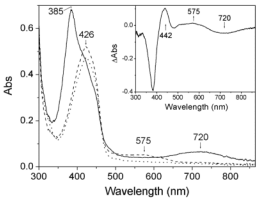

Figure 1.

Visible spectra of the MCR_{BES} radical. Visible spectrum of 21 μM MCR_{red1} (61%) (solid line) in the presence of 500 μM CoB_6SH 30 s (dashed line) and 1 h (dotted line) after addition of 2 mM BES. The inset is the difference spectrum (the 30 s spectrum minus the spectrum before addition of BES).

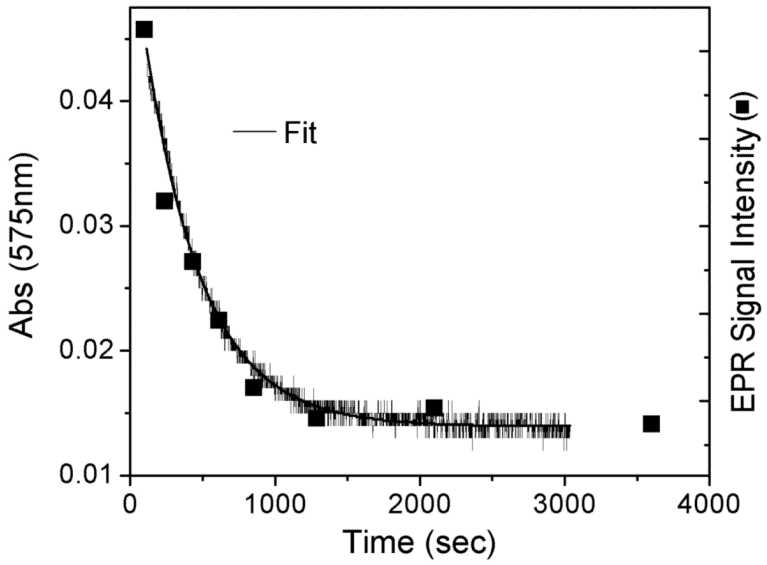

Figure 2.

Slow kinetics of MCR_{BES} radical decay after reaction of MCR_{red1} with BES in the presence of CoB_6SH followed by visible (left) and EPR spectroscopy (squares). The EPR signal intensity of the MCR_{BES} radical was measured after freeze quenching the reaction at various times. EPR parameters: microwave frequency, 9.384 GHz; microwave power, 10.440 mW; modulation frequency, 100 kHz; modulation amplitude, 10 G and temperature, 70 K. The calculated values were: k_{obs} of 0.0021 ± 0.003 s^{-1} (UV-visible) or 0.0021 ± 0.0003 s^{-1} (EPR).

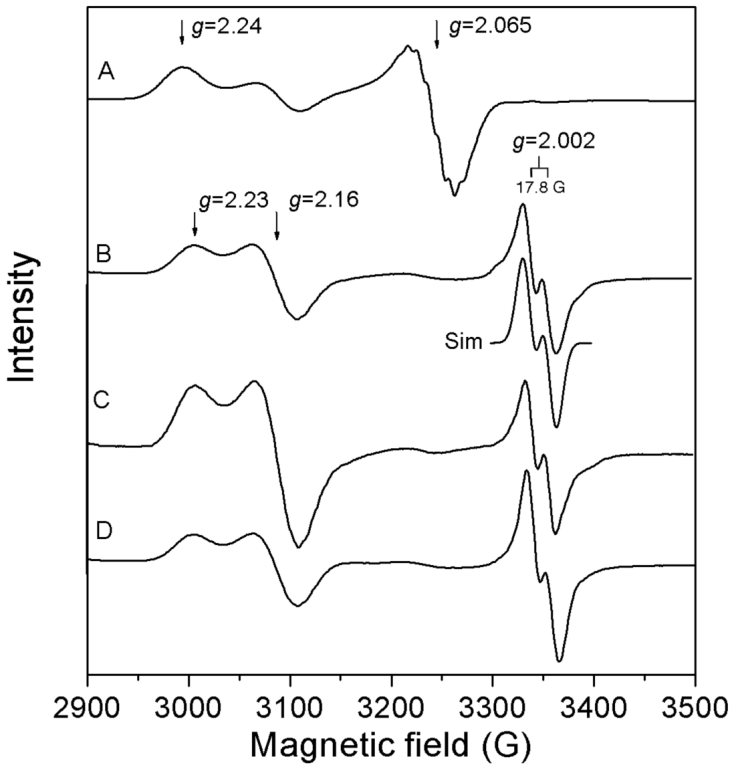

Figure 3.

EPR spectra of 150 μM MCR_{red1} (A) after addition of 1.5 mM CoB_6SH and 1.5 mM BES in H_2O (B) and D_2O (C). The EPR spectrum in (D) was obtained after reacting MCR_{red1} containing universally labeled $^2H_6$-Tyr residues under identical conditions as in (B). EPR parameters: microwave frequency, 9.384 GHz; microwave power, 10.440 mW; modulation frequency, 100 kHz; modulation amplitude, 10 G and temperature, 70 K.

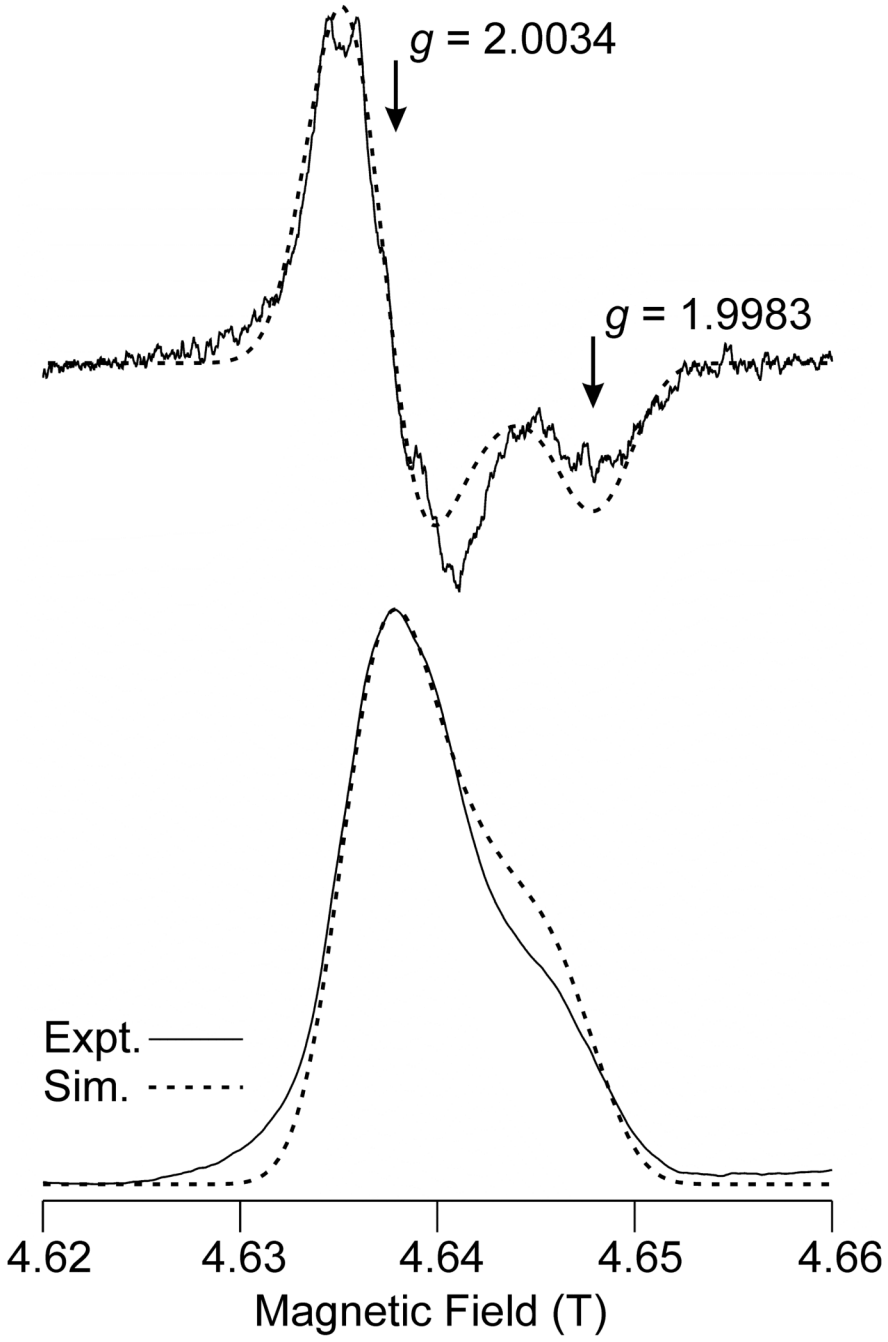

Figure 4.

High Frequency (130 GHz) two-pulse (Hahn) echo-detected EPR spectrum of MCR_{red1} reacted with CoB_6SH and BES for 1 min and then frozen. The derivative of the spectrum is also presented (upper trace) to approximate the effects of field modulation in a CW experiment. Acquisition parameters: temperature: 7 K; repetition rate: 30 Hz; number of acquisitions per point: 840; 90 degree pulse width: 40 ns; time between pulses: 150 ns; scan time: 200 s; number of scans: 28, EPR frequency: 130.001 GHz. Simulation parameters: **g** = [2.00340, 2.00340, 1.99832]; single-crystal Gaussian linewidths (hwhm), W = 60, 60, 50 MHz; isotropic hyperfine coupling to a single ^1H with A = 50 MHz was also included, but this has a barely perceptible effect on the spectral appearance.

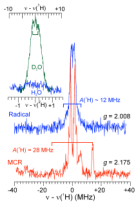

Figure 5.

Broad scan "stochastic" CW 35 GHz ^{1}H ENDOR spectra recorded at 2 K of MCR_{red1} in the presence of 1 mM CoB_6SH after addition of BES at a field position on the radical signal (blue trace; g = 2.008) and at one on the MCR signal (red trace; g = 2.175). The latter exhibits a signal from a strongly coupled ^{1}H that has been denoted as H_{rh} by Harmer et al. and fully analyzed by them.(47) Experimental conditions: microwave frequency, 35.013 GHz; modulation frequency, 1 G; microwave power, 30 dB (~10 μW); random hopping of rf with delay time: 1 ms, sample time: 1 ms, rf time: 1 ms; 400 scans. The inset shows 35 GHz ^{2}H Mims ENDOR spectra at 2 K of MCR_{red1} in H_2O solvent (blue trace) and D_2O solvent (green trace). The spectra are centered at the ^{2}H Larmor frequency (8.1 MHz) with a scale in ^{2}H coupling, but a scale in corresponding ^{1}H coupling is also shown. Experimental conditions: microwave frequency, 34.895 GHz (D_2O), 34.851 GHz (H_2O); π/2 pulse width = 50 ns; delay time, τ = 600 ns; magnetic field, 1.2418 T (g = 2.0077 (D_2O); 2.0052 (H_2O)); repetition time, 20 ms; random hopping of rf; 50 scans.

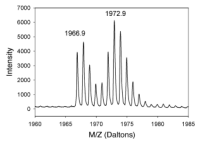

Figure 6.

Mass spectrum of the fragment containing βTyr367 (IYGGGGPGIFNGNHIVTRH), which is located directly above the Ni center in F_{430}. MCR isolated from *M. marburgensis* cells was digested with BrCN and AspN.

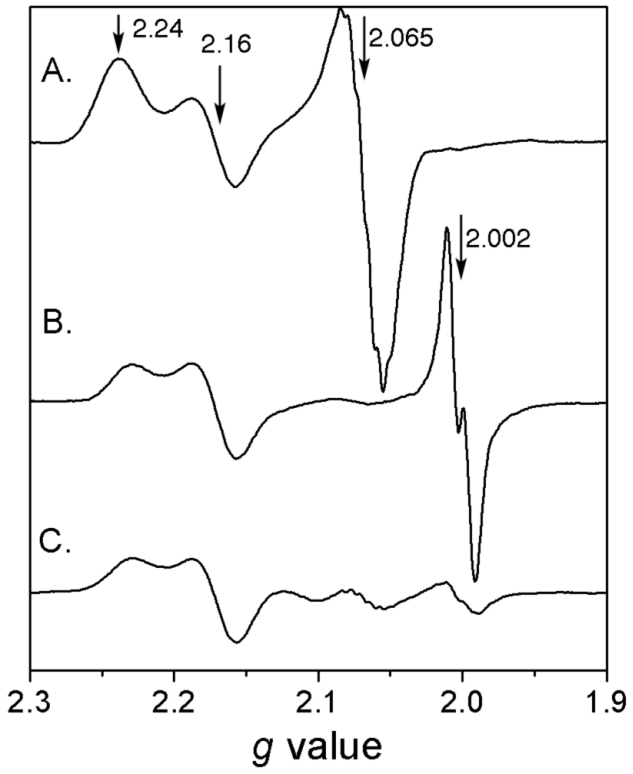

Figure 7.

X-band EPR spectra of 100 μM MCR_{red1} after reaction with (A) acetyl-imidazole, (B) with 5 mM BES in presence of 1 mM CoB_6SH, and (C) with 5 mM BES and 1 mM CoB_6SH (as in B) and acetyl-imidazole. EPR parameters: microwave frequency, 9.384 GHz; microwave power, 10.440 mW; modulation frequency, 100 kHz; modulation amplitude, 10 G and temperature, 70 K.

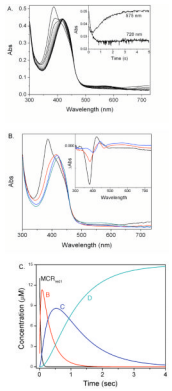

Figure 8.

(A) Time-course of the reaction of 15 μM MCR_{red1} with 5 mM BES in the presence of 110 μM CoB_6SH (interval 0.1 s). The Insert shows the absorbance changes at 575 and 720 nm. (B) Visible spectra of MCR_{red1} plus CoB_6SH (black line), the trapped intermediate B (red line), the trapped intermediate C (blue line) and Intermediate D (including the MCR_{BES} radical, green line) by global fitting the data in (A) to four-component reaction. Insert: The difference spectra of intermediate B minus MCR_{red1} (black line), intermediate B minus intermediate C (red line) and MCRred1 minus intermediate C (blue line). (C) The time-course of the changes in the concentrations of MCR_{red1} (black line), intermediate B (red line), intermediate C (blue line) and Intermediate D, the MCR_{BES} radical (green line) upon the reaction in (A).

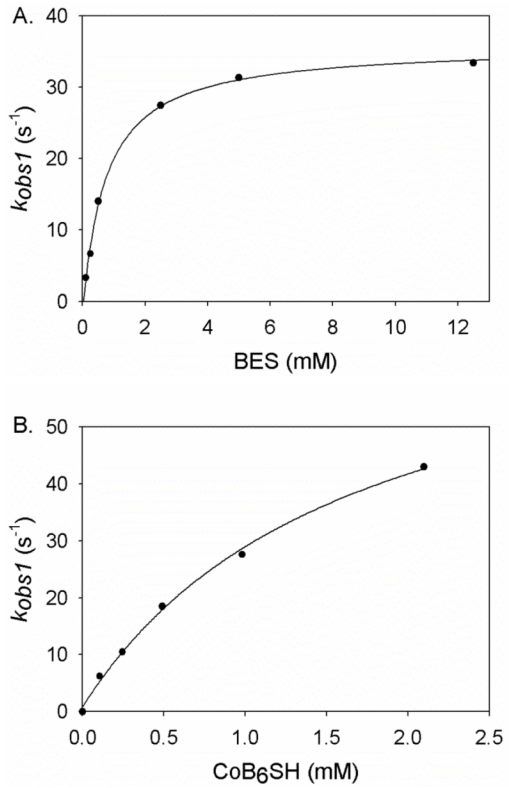

Figure 9.

Concentration dependence of the rate of MCR_{BES} radical formation (A) Dependence of MCR_{BES} radical formation on the concentration of BES. A solution containing 15 μM MCR_{red1} (58%) and 1 mM CoB_6SH was reacted with varied concentrations of BES at room temperature. (B). CoB_6SH concentration dependence of MCR_{BES} radical formation. The mixture of 15 μM MCR_{red1} (58%) and various concentration of CoB_6SH was shot against 5 mM BES at room temperature. Reported rate constants are the average of three to four different rapid-mixing experiments.

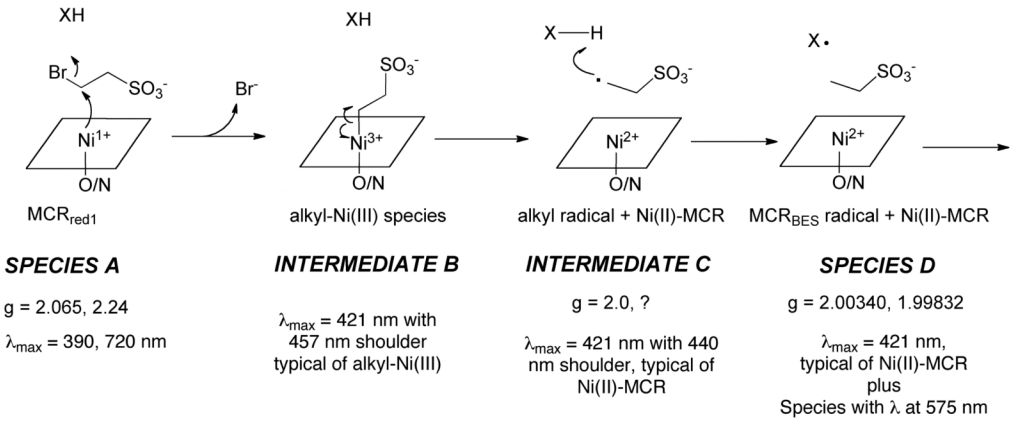

Figure 10.

Proposed mechanism for MCR_{BES} radical formation. "X" is the species with the doublet radical EPR spectrum and the long wavelength absorption. Further isotope substitution and spectroscopic experiments are required to identify "X", as described in the text.

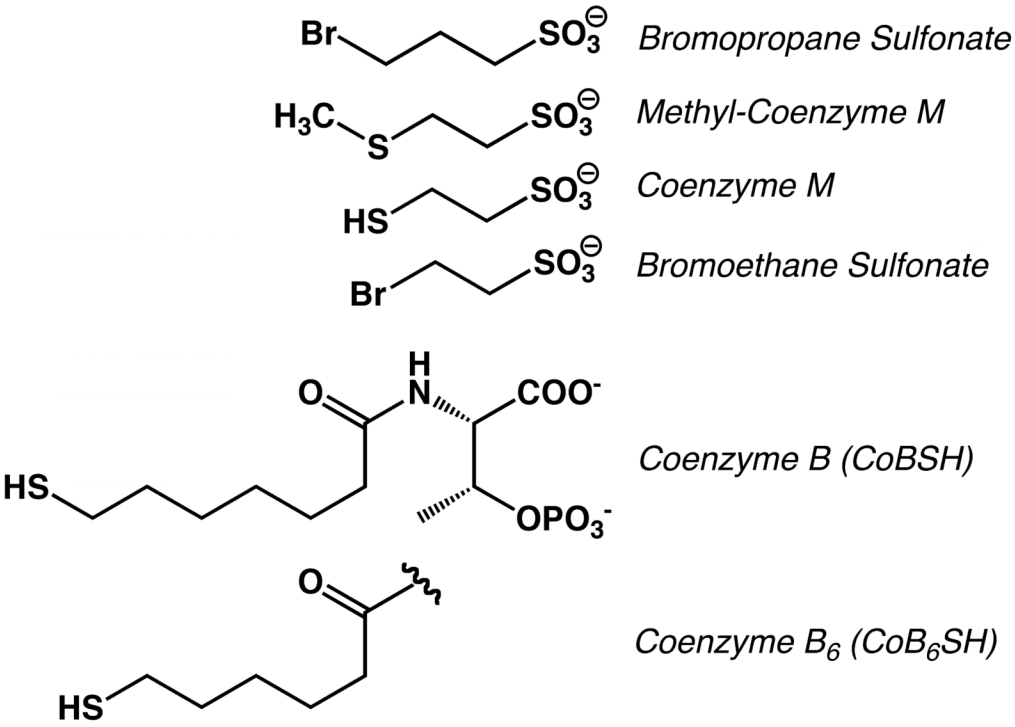

Scheme 1.
Structures of HSCoM analogs.

Table 1

Kinetic parameters for the three-step reaction involving MCR_{red1} radical formation

	k_1 $A \rightarrow B$			k_2 $B \rightarrow C$	k_3 $C \rightarrow D$
	k_1 (s^{-1})	K_{m1} (mM)	k_1/K_{m1} ($M^{-1}s^{-1}$)	k_2 (s^{-1})	k_3 (s^{-1})
CoB_6SH (with 5 mM BES)	75 ± 6	1.7 ± 0.3	45000 ± 9000	2.6 ± 0.3	1.0 ± 0.1
BES (in presence of 1 mM CoB_6SH)	38 ± 1	0.7 ± 0.1	51500 ± 9900	2.8 ± 0.5	1.1 ± 0.1